Hybrid-Driven High-Resolution Prestack Seismic Inversion

Jian Zhang, Xiaoyan Zhao, Hui Sun, Jingye Li, and Xiaohong Chen

***Abstract*—Prestack seismic inversion is considered among the most frequently utilized techniques for reservoir characterization. However, the resolution of the inverted parameters, such as P-, S-wave velocity, and density, is low due to the limited bandwidth and side-lobe interference of the seismic wavelet. To address this issue, a hybrid two-step strategy that combines data-driven and model-driven methods is proposed to enable higher resolution and accuracy of the inverted results. We first construct a three-layer fully connected network to implement the mapping of seismic data to reflection coefficients. The method does not require exact seismic wavelet to be known and intensive human-computer interaction. It estimates reflectivity based on the extracted features from training data, which gives more accurate results compared with traditional sparse inversion methods. Then, the model-driven method (i.e., amplitude variation with offset/angle inversion method) is adopted to reconstruct P-wave velocity, S-wave velocity, and density from the estimated reflection coefficients. The performance of the hybrid-driven strategy is checked using synthetic model and real data. The results indicate that the proposed method provides more accurate and higher resolution inversion results for seismic reservoir characterization.**

***Index Terms*—Data-driven, model-driven, prestack inversion, reservoir characterization.**

I. Introduction

THE accuracy of reservoir characterization usually relies on the analysis of subsurface attributes (e.g., velocity, density, and impedance). Amplitude-variation-with-offset/angle inversion is a frequent methodology to obtain velocity and density from recorded seismogram [1], [2], [3], [4]. Due to the advantage of low cost, the convolutional model is still the most widely used method in the oil or gas industry, i.e., the seismic record is represented by convolving the reflection coefficient with seismic wavelet [5]. The relationship between the elastic parameters and the reflection coefficient can be characterized by the Zoeppritz equation [6]. However, the nonlinearity of the equation leads to some difficulties in applications such as interpretation and inversion [7]. Therefore, in the past decades, many scholars have developed various linear approximations [8], [9]. Although reflection coefficients provide important information on subsurface parameters, the band-limited wavelet and observation noise increase the difficulty of predicting elastic parameters using observed seismic data.

Improving the resolution of inversion results has long been a focus and difficult area of research in reservoir characterization. Stochastic inversion and sparsely constrained deterministic inversion are the most commonly used methods to recover high-resolution results from seismic data. Stochastic inversion methods can produce high resolution inversion results, however, the expensive computational costs limit their use in practice [2], [10], [11], [12]. Deterministic inversion methods based on sparse constraints are widely adopted in practical applications as an alternative to provide high-resolution inversion results due to the low cost. The sparse constraints including Cauchy regularization, L_1 norm regularization, and differential Laplace regularization are often integrated into inversion algorithm to reconstruct high-resolution elastic parameters directly from measured data [13], [14], [15], [16]. However, it is clear from the logging data that the true subsurface parameter is continuous and not sparse-spike [17]. Besides, it is difficult to remove the bandwidth limitation effects of the wavelet when calculating elastic parameters directly from seismic data. Well-bore-dependent reflectivity analysis shows that the main strata units are associated with sparse reflection coefficients [18]. Moreover, as shown by the exact Zoeppritz equation and its approximations, the elastic parameter is directly related to the reflection coefficient.

The sparse-spike deconvolution technique reconstructs the reflection coefficients by attempting to circumvent the defects of seismic wavelet on the recorded seismograms [19], [20], [21]. Least square (LS) algorithms with L_1 norm regularization are widely used to recover sparse results [22], [23]. However, the method has demanding requirements for the seismic wavelet, i.e., a small deviation between the input wavelet and the actual wavelet will lead to a large deviation between the prediction and the actual value. Besides, the method requires extensive human-computer interaction for the adjustment of hyper-parameters to obtain the best prediction results. These problems greatly limit the application of the method in practice and make it more

Manuscript received 16 July 2023; revised 19 September 2023; accepted 8 October 2023. Date of publication 11 October 2023; date of current version 23 October 2023. This work was supported in part by the Natural Science Foundation of China under Grant 42204108, in part by the Natural Science Foundation of Sichuan under Grant 2023NSFSC0768, in part by the Fundamental Research Funds for the Central Universities under Grant 2682022CX030, and in part by the Research and Development Department, China National Petroleum Corporation-Investigations on Fundamental Experiments and Advanced Theoretical Methods in Geophysical Prospecting Applications under Grant 2022DQ0604-04. *(Corresponding author: Hui Sun.)*

Jian Zhang, Xiaoyan Zhao, and Hui Sun are with the Faculty of Geosciences and Environmental Engineering, Southwest Jiaotong University, Chengdu 611756, China, and also with MOE Key Laboratory of High-Speed Railway Engineering, Southwest Jiaotong University, Chengdu 610036, China (e-mail: zhangjian93@swjtu.edu.cn; xyzhao2@swjtu.edu.cn; sunhui@swjtu.edu.cn).

Jingye Li and Xiaohong Chen are with the State Key Laboratory of Petroleum Resources and Prospecting, National Engineering Laboratory for Offshore Oil Exploration, China University of Petroleum-Beijing, Beijing 102249, China (e-mail: lijingye@cup.edu.cn; chenxh@cup.edu.cn).

Digital Object Identifier 10.1109/JSTARS.2023.3323696

difficult to apply. As computational power and its corresponding algorithms continue to improve, data-driven methods, including machine learning or deep learning, are being implemented successfully in diverse fields, especially computer vision and image processing [24]. Data-driven methods are also widely used in certain geosciences, such as denoising [25], [26], [27], seismic inversion [28], [29], [30], resolution enhancement [31], fault detection [32], lithology prediction [33], [34], [35], and horizon picking [36]. The method deals with inverse problems by learning and mining valid information from massive training datasets based on statistical technologies. However, data-driven seismic inversion is difficult as there are such a limited amount of known wells. In contrast, the reflection coefficients can be represented using random sequences, so it is easy to construct training data. In addition, once the network training is completed, its prediction takes much less time than those by the LS-based approach.

In this article, we develop a hybrid-driven inversion strategy to improve the estimation of P-, S-wave velocity, and density. The data-driven method (i.e., fully connected neural network-FCN) is first performed to reconstruct the reflectivity from recorded seismograms. Then, a model-driven inversion algorithm based on the Aki-Richard formula is adopted to calculate elastic parameters from the reconstructed reflectivity. The combination of these two methods overcomes, to some extent, the drawbacks when either method is used alone. We demonstrate the advantages of the proposed algorithm by implementing it on synthetic data sets and a field case. The results demonstrate that the proposed approach provides more accurate and higher resolution inversion results than the conventional seismic inversion.

II. Method

A. Reflectivity Inversion

To date, the convolutional model is still the most frequently used method in the oil and gas business, i.e., the seismogram is obtained by convolving the reflection coefficient with seismic wavelet. Using the matrix notation, the angle gather can be denoted as follows:

$$\mathbf{d}(\theta_i) = \mathbf{W} \cdot \mathbf{r}(\theta_i) + \mathbf{e}(\theta_i), \quad i = 1, 2, \cdots, n \tag{1}$$

where $\mathbf{d}(\theta_i)$ denotes the seismogram associated with the i_{th} angle of incidence θ_i, $\mathbf{W}$ denotes the wavelet convolutional matrix, $\mathbf{r}(\theta_i)$ denotes the reflectivity associated with the i_{th} angle of incidence θ_i, $\mathbf{e}(\theta_i)$ denotes the random noise in the observation, and n denotes the number of angles. The objective of reflectivity inversion is to reconstruct the reflection coefficients $\mathbf{r}(\theta_i)$ for given seismic data $\mathbf{d}(\theta_i)$. However, the inversion is usually ill-posed due to the negative effects (e.g., limited bandwidth and side-lobe disturbances) of seismic wavelet $\mathbf{W}$ and noise $\mathbf{e}(\theta_i)$.

B. Data-Driven Algorithm

Deep neural network (DNN), as a data-driven approach, is effective for solving the inverse problem. The method deals with inverse problems by learning and mining valid information from massive training datasets using a human-like brain neuronal behavior. For data-driven reflectivity inversion (DDRI), some samples of the reflection coefficients $\mathbf{r}$ (i.e., labels) and the measured seismic records $\mathbf{d}$ (i.e., inputs) are offered to obtain a mapping function, which is then used to implement the converter of seismic data to reflection coefficients. The objective function of DDRI is expressed as follows:

$$J = ||\mathbf{r} - \mathcal{G}_\Theta(\mathbf{d})||_2^2 \tag{2}$$

where $\mathcal{G}_\Theta$ represents the mapping function that converts the seismic data $\mathbf{d}$ into reflection coefficients $\mathbf{r}$, and Θ represents the ensemble of parameters including weights and biases that need to be optimized during the training process. There are two key factors to consider for a data-driven approach to be successful. One is the network framework and the other is the training dataset.

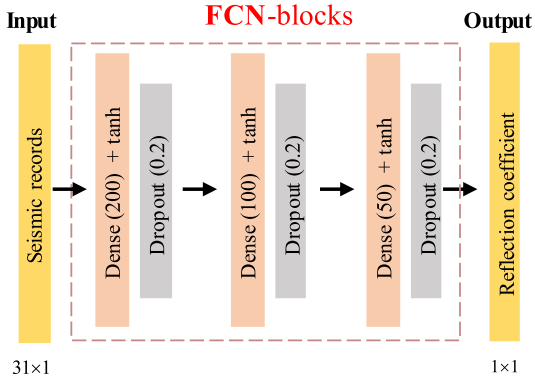

Fig. 1. Schematic representation of the adopted neural network framework. The input consist of a tensor of size 31×1. The corresponding output is actual reflection coefficient of size 1×1. The intermediate rectangles indicate the key layers of the network.

A DNN usually has an input layer and an output layer with multiple hidden layers in between. In this article, we build a reliable DNN framework through a trial-and-error strategy. By adjusting the number of network layers and the corresponding number of neurons, the relative optimal network is obtained by considering the balance between cost and performance. The network is called a fully connected neural network (FCN) and contains three fully connected layers except for the input and output layers. Fig. 1 shows the details of network architecture used for reflectivity inversion. The samples of input consist of a tensor of size 31×1, the size of which is variable in terms of the dominant frequency of seismic data. The choice of size will be explained in more detail during the construction of the training data. The three fully connected layers have 200, 100, and 50 neuron units, respectively. The output is the reflectivity value of dimension 1×1. There is a dropout layer behind each fully connected layer to prevent overfitting. After each layer (except for the last one), we use the tanh activation function. Since the reflectivity inversion is a regression problem, the adaptive moment estimation (ADAM) method is employed to minimize the mean square error (MSE) between the predicted values and the labels in order to obtain optimal network parameters Θ. We set the batch size and epochs to 16 and 1000, respectively. During the training process, 16.7% of the input datasets are utilized as the validation datasets.

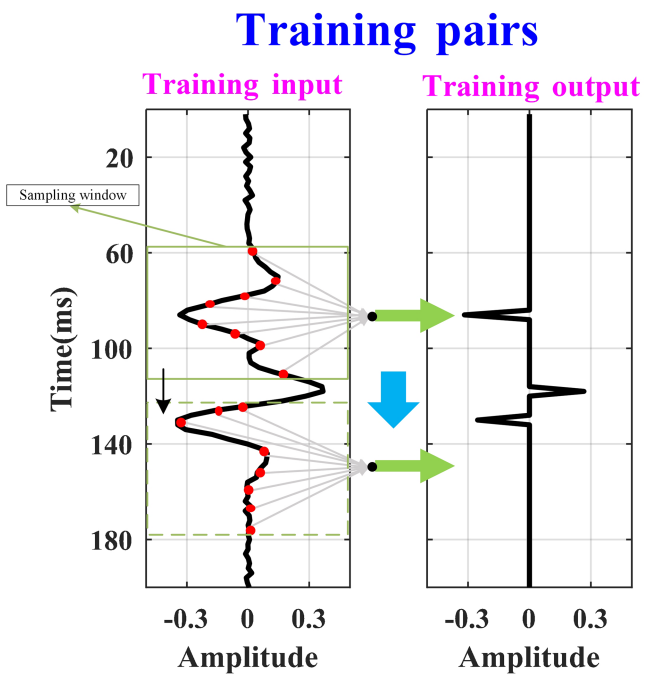

Fig. 2. Schematic diagram of training data pairs construction.

An effective training dataset is another important factor in the success of data-driven approaches. One can use any existing or synthetic dataset as a training dataset for data-driven methods, if these training datasets are well-representative of the distribution of the observed data. In this article, a total of 5000 reflectivity models are generated randomly. In each reflectivity model, there are three reflectors with different amplitudes and positions. A possible reflectivity model is shown on the right in Fig. 2, i.e., the output of the training. Then, the corresponding seismic record is obtained by convolving with the zero-phase Ricker wavelet. The central frequency of wavelet for the synthetic dataset is 26–34 Hz. For field data sets, different seismic wavelets are obtained using Hampson–Russell software (HRS). Meanwhile, different degrees of Gaussian white noise are mixed to obtain the training input (the left of Fig. 2). A sampling window of a specific size (31 points with 2 ms intervals) is used to split the training input (the left of Fig. 2) to form the small patches (red dots in the left of Fig. 2), thus obtaining the input to the network. The output of the network corresponding to a small patch is the reflectivity (the right of Fig. 2) at its center. A small patch and its corresponding reflectivity form a training pair. By scanning the sampling window in turn, we can generate many training pairs (Fig. 2). Since the minimum central frequency of the wavelet in our experiments is 26 Hz, the small patch obtained with a sampling window of 31 points (62 ms >40 ms) is sufficient to characterize a complete wavelet.

Compared with data-driven algorithms, the objective function of model-driven reflectivity inversion (MDRI) is expressed as follows:

$$J = ||\mathbf{d} - \mathbf{W}\mathbf{r}||_2^2 + \lambda||\mathbf{r}||_1 \tag{3}$$

where $||\cdot||_2^2$, $||\cdot||_1$ represent L_2 norm and L_1 norm regularization, respectively. The L_2 norm leads to stable and smooth solutions. However, the L_1 norm facilitates sparse solutions as opposed to the L_2 norm. λ is a non-negative regularization parameter that trade-off the data matching and sparsity of the inversion results. As can be seen from (3), the model-driven inversion method requires known seismic wavelet $\mathbf{W}$ and appropriate parameter λ. However, both the seismic wavelet $\mathbf{W}$ and the regularization parameter λ are difficult to be to be accurately obtained in practice.

C. Single-Step Model-Driven Inversion (SSMI) for Three Parameters

The reflection coefficient is related to the properties of the subsurface material (e.g., Vp, Vs, and density). Under the weak contrast assumption, the dependence of the reflection coefficient on the elastic parameters can be expressed as follows [8]:

$$r(\theta) = a(\theta)\frac{\Delta\rho}{\bar{\rho}} + b(\theta)\frac{\Delta Vp}{\bar{V}p} + c(\theta)\frac{\Delta Vs}{\bar{V}s}. \tag{4}$$

And,

$$\begin{aligned} a(\theta) &= \frac{1}{2}\left(1 - 4\frac{\bar{V}s^2}{\bar{V}p^2}\sin^2\theta\right),\ b(\theta) = \frac{\sec^2\theta}{2},\\ c(\theta) &= -4\frac{\bar{V}s^2}{\bar{V}p^2}\sin^2\theta,\\ \bar{V}p &= (Vp_1 + Vp_2)/2,\ \bar{V}s = (Vs_1 + Vs_2)/2,\\ \bar{\rho} &= (\rho_1 + \rho_2)/2,\\ \Delta Vp &= Vp_2 - Vp_1,\ \Delta Vs = Vs_2 - Vs_1,\ \Delta\rho = \rho_2 - \rho_1,\\ \theta &= (\theta_1 + \theta_2)/2 \end{aligned} \tag{5}$$

where θ_1, θ_2 represent the angle of incidence and transmission of P-wave, respectively. $Vp_1, Vp_2, Vs_1, Vs_2, \rho_1, \rho_2$ represent the P-wave velocity, S-wave velocity, and density in the two layers above and below the interface.

Based on Taylor's formula, the single-interface reflection coefficient in (4) can be rewritten as follows:

$$\begin{aligned} r(t,\theta) = a(\theta)\frac{\partial}{\partial t}\ln(\rho(t)) + b(\theta)\frac{\partial}{\partial t}\ln(Vp(t))\\ + c(\theta)\frac{\partial}{\partial t}\ln(Vs(t)). \end{aligned} \tag{6}$$

In matrix notation, (6) can be expressed as follows:

$$\mathbf{r} = \mathbf{F}\mathbf{D}\mathbf{m} = \mathbf{G}\mathbf{m} \tag{7}$$

where $\mathbf{F}$ is a sparse matrix that contains $a(\theta)$, $b(\theta)$, $c(\theta)$. $\mathbf{D}$ represents the derivative matrix.

The objective function based on model-driven to predict the elastic parameters is expressed as follows:

$$J = \frac{1}{2}\left(||\mathbf{d} - \mathbf{W}\mathbf{G}\mathbf{m}||_2^2 + \lambda||\mathbf{m} - \mathbf{m_0}||_2^2\right) \tag{8}$$

where $\mathbf{m}_0$ represents the low-frequency model of the three parameters from well-logs data. However, the negative effects (e.g., limited bandwidth and side-lobe disturbances) of

wavelet $\mathbf{W}$ reduces the resolution and accuracy of the inverted elastic parameters. λ is a non-negative regularization parameter.

Combining DDRI and SSMI, the objective function for predicting the elastic parameters based on the hybrid-driven strategy (HDS) is expressed as follows:

$$J = \frac{1}{2}(||G_\Theta(\mathbf{d}) - \mathbf{Gm}||_2^2 + \lambda||\mathbf{m} - \mathbf{m_0}||_2^2) \tag{9}$$

where $\mathcal{G}_\Theta$ represents the trained DNN used to eliminate the negative effects (e.g., limited bandwidth and side-lobe disturbances) of seismic wavelet. λ is a non-negative regularization parameter.

The derivatives of the objective function (9) with respect to the model parameters are obtained

$$\frac{\partial J}{\partial m} = \mathbf{G}^T(G_\Theta(\mathbf{d}) - \mathbf{Gm}) + \lambda(\mathbf{m} - \mathbf{m_0}). \tag{10}$$

Solving for the minima of the objective function is equivalent to making its derivative equal to zero, which leads to the following equation:

$$\mathbf{m} = (\mathbf{G}^T\mathbf{G} - \lambda\mathbf{I})^{-}(\mathbf{G}^T G_\Theta(\mathbf{d}) - \lambda\mathbf{m_0}) \tag{11}$$

where $\mathbf{I}$ represents the identity matrix.

III. Application

In this subsection, we validate the proposed methodology using synthetic model and actual data. In the subsequent experiments, the DDRI is referred to as DDRI, the MDRI is referred to as MDRI. The single-step model-driven seismic inversion is denoted as SSMI, and the proposed hybrid-driven strategy for elastic parameter prediction is denoted as HDS. The method of taking DDRI-based results as input is noted as DHDS and the method of taking MDRI-based results as input is noted as MHDS. We first demonstrate the advantages of the DDRI approach over MDRI using synthetic data, and then the results obtained based on DDRI are used for the prediction of elastic parameters. Finally, the proposed methodology is implemented on actual data to further verify the effectiveness of the proposed method.

A. Synthetic Data Example

To prove the validity of the proposed method, we first generate a single trace reflectivity model containing four reflectors as well as two wedge models. Our experiments focus on the signal-to-noise ratio (SNR), the error of seismic wavelet, and the tuning thickness to demonstrate the advantages of DDRI over MDRI. The single trace reflectivity model is shown in Fig. 3 and is used to verify the effect of noise and wavelet errors on the performance of the methods. Fig. 4(a) shows the effect of noise on the inversion results of DDRI and MDRI. As the SNR increases, the performance of the inversion results of the two methods gradually increases, and when the SNR reaches 10, the performance of the two methods is comparable. However, the performance of DDRI is significantly better than that of MDRI at low SNRs. Fig. 4(b) shows the effect of wavelet on the inversion results of DDRI and MDRI. It can be seen that the traditional reflectivity inversion method (i.e., MDRI) relies heavily on the accuracy of wavelet, whereas the data-driven method (i.e., DDRI) is less affected by wavelet. In this context, the relative error refers to the difference of the dominant-frequency between the wavelet used and the true wavelet.

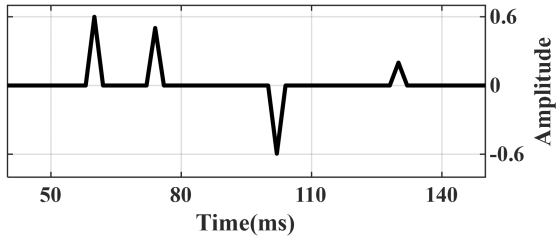

Fig. 3. Single trace reflectivity model.

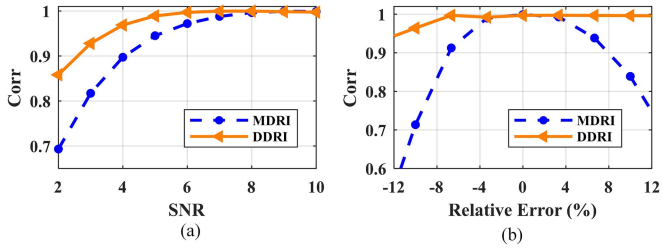

Fig. 4. Effects of (a) SNR and (b) wavelet error for different methods.

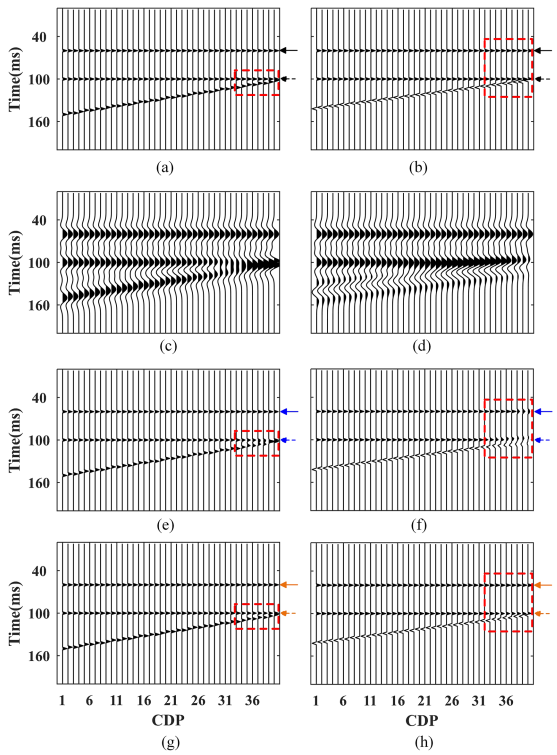

Fig. 5. Tests of wedge models with one horizontal layer. (a) Two reflectors of wedge model with positive values. (b) Two reflectors of wedge model, one positive and one negative. (c) and (d) Synthetic seismic records are obtained by convolving a given source wavelet and the reflectivity shown in (a) and (b), respectively. (e) and (f) Inverted reflectivity using MDRI, respectively. (g) and (h) Inverted reflectivity using DDRI, respectively.

Furthermore, the wedge model is used to test the predictability of both methods for thin layers. Fig. 5 shows inverted reflectivity

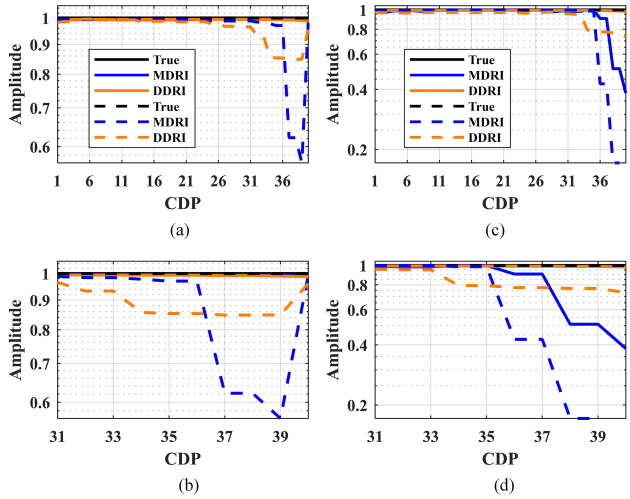

Fig. 6. Comparison of peak amplitudes. (a) Extracted from arrows shown in Fig. 5(a). (e). (g). Zoom view (b) from (a). (b) Extracted from arrows shown in Fig. 5(b). (f). (h). Zoom view (d) from (c).

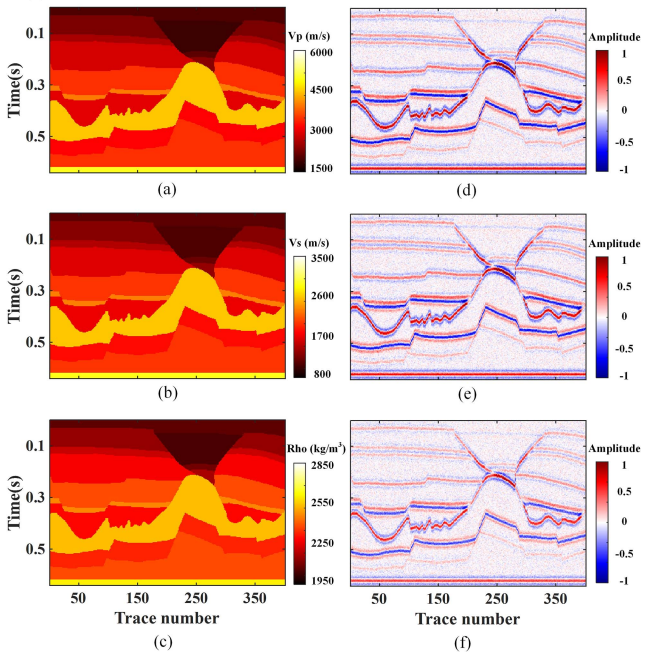

Fig. 7. BP models of (a) P-wave velocity, (b) S-wave velocity, and (c) density. And, the angle gathers from the BP model with SNR = 5 of (d) 5°, (e) 15°, and (f) 25°.

using DDRI and MDRI. In this example, two wedge models are included, namely, two reflection coefficients that are both positive [Fig. 5(a)] and two reflection coefficients that are one positive and one negative [Fig. 5(b)]. Also, we have added a horizontal layer to the wedge model to analyze the effect of the wedge model on it during the inversion. A zeros-phase Ricker wavelet with a central frequency of 30 Hz is used as the source. The synthetic seismic records [Fig. 5(c) and (d)] are then obtained by convolving the reflectivity [Fig. 5(a) and (b)] with the known source.

The inverted results of reflectivity using MDRI are shown in Fig. 5(e) and (f). In Fig. 5(e), the thin layer (red box) is not well-identified. In Fig. 5(f), the inverted reflectivity gives a good indication of the thin layer, but the position is wrong. And, it affects the inversion results of the overlying layers. The inverted results [Fig. 5(g) and (h)] of reflectivity using DDRI show better accuracy than those of MDRI. For further comparison, we show the peak amplitudes of the different inversion results, as shown in Fig. 6. Fig. 6(a) shows the comparison of the peak amplitudes for the even reflectivity pairs, while a zoomed-in view is displayed in Fig. 6(b). Fig. 6(c) displays the comparison of the peak amplitudes for the odd reflectivity pairs, while a zoomed-in view is shown in Fig. 6(d). Overall, the inversion results of DDRI are in better agreement with the true values than those of MDRI.

The BP model [Fig. 7(a)–(c)] is adopted as an example for inversion of elastic parameters. The corresponding 5°, 15°, and 25° profiles (SNR = 5) are shown in Fig. 7(d)–(f). The wavelet used here is the same as the one used in the previous example. The low frequency models of Vp, Vs, and density are displayed in Fig. 8(a)–(c).

Fig. 8(d)–(f) display the inverted Vp, Vs, and density of SSMI. Although the inverted results of SSMI reveal the general architecture of the strata, the layer boundaries as well as the thin layers are blurred. The inversion results of MHDS [Fig. 9(a)–(c)] and DHDS [Fig. 9(d)–(f)] show higher resolution compared with the results of SSMI, but the results of DHDS are optimal.

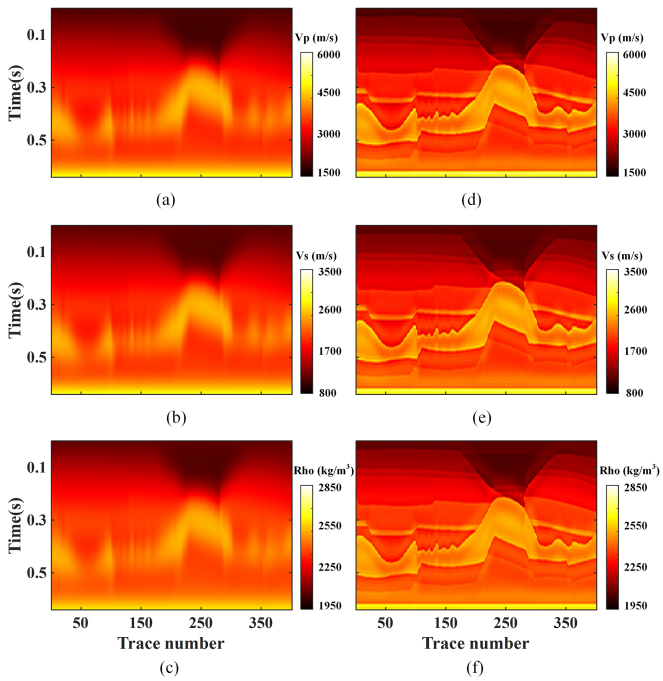

Fig. 8. Low frequency models of (a) Vp, (b) Vs, and (c) density. And, the inverted results derived using SSMI. (d) Vp, (e) Vs, and (f) density.

This is consistent with the conclusion of our previous tests, i.e., the DDRI obtains better results compared with MDRI. The root-mean-square error (RMSE) is introduced to quantitatively assess the results. Table I shows the RMSE between the true and the inverted results of the three methodologies for the full BP model. In agreement with our previously obtained conclusions,

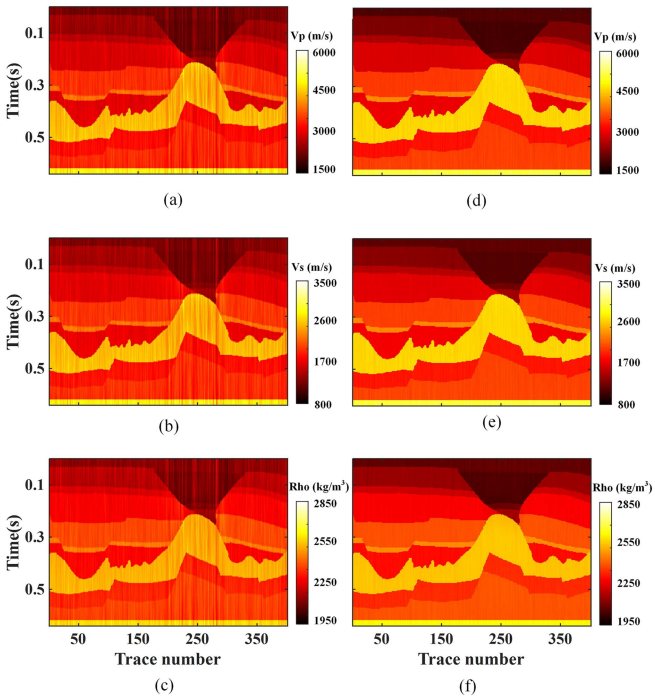

Fig. 9. Inverted results obtained using MHDS (a) Vp, (b) Vs, and (c) density. And, the inversion results obtained using DHDS (d) Vp, (e) Vs, and (f) density.

TABLE I
RMSE BETWEEN THE TRUE AND THE INVERTED RESULTS OBTAINED FROM SSMI, MHDS, AND DHDS FOR THE FULL BP MODEL (SNR = 5)

	Vp	Vs	Rho
SSMI	272.44	157.29	44.32
MHDS	179.27	103.50	36.30
DHDS	79.19	45.72	9.30

the HDS methods produce better inversion results, but DHDS is optimal. The magnitudes of RMSE for Vp, Vs, and density varies depending on the range of values they take.

In order to compare the differences between the inverted of the three methods in further detail, a comparative view of a single-trace is shown in Fig. 10. The results of SSMI (the orange dotted lines with solid dot) are agreement with the tendency of the true values, but the parameter values are incorrectly estimated within some layers and the boundaries of the layers are not well-characterized. The results of MHDS (the blue dashed lines) deviate from the true values at some locations due to the limited accuracy of the reflection coefficients obtained from MDRI, but match the true values more closely and characterize the layer boundaries more accurately. The inversion results (the green dashed-dotted lines) of DHDS match the reference model better than the other two methods, resulting in a more reliable inversion profile [Fig. 9(d)–(f)]. In addition, a comparison of the RMSE of the results recorded in Table II shows that DHDS has the smallest RMSE.

B. Real Data Example

Encouraged by the synthesized experimental numerical results, a trial is conducted utilizing field data from north-western

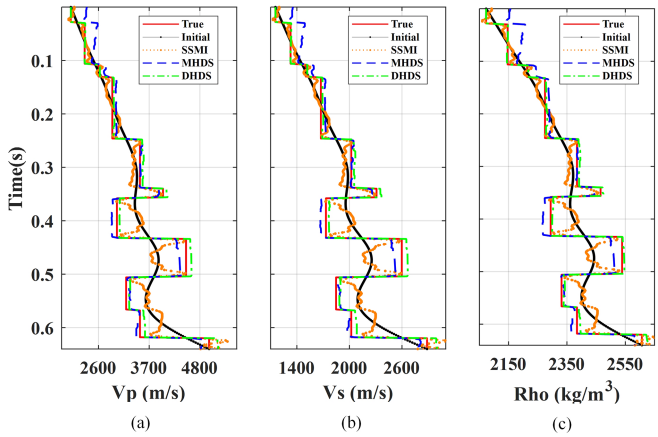

Fig. 10. Synthetic test of single-trace data. (a) Inverted Vp using SSMI, MHDS, and DHDS. (b) Inverted Vs using SSMI, MHDS, and DHDS. (c) Inverted density using SSMI, MHDS, and DHDS.

TABLE II
RMSE BETWEEN THE TRUE AND THE INVERTED RESULTS OBTAINED FROM SSMI, MHDS, AND DHDS FOR THE SINGLE-TRACE DATA

	Vp	Vs	Rho
SSMI	308.33	178.01	49.87
MHDS	139.67	80.64	29.48
DHDS	73.55	42.46	7.52

China. The selected crossing-well section comprises 401 traces and 200 samples sampled at an interval of 0.002 s and the target zone is defined from 1.7 to 2.1 s. Fig. 11(a)–(c) show the partially stacked profiles, denoted as small, middle, and large angle gathers with angle from 0°–10°, 10°–20°, and 20°–30°, respectively. Frequency spectrum analysis shows that the dominant frequency of the seismic data in the study area is about 25 Hz and the effective frequency band is 5–55 Hz. Although this real data has been preprocessed using de-noising, static correction, and amplitude compensation, the partially stacked profiles still have noise as well as limited resolution due to the complexity of the surface undulations. One well is available in the selected crossing-well section to validate the trustworthiness of the inversion. The well-location (blue line) is also projected in Fig. 11. The low frequency initial models of Vp, Vs, and density (Fig. 12) are built from the real data using the initial model building module of the HRS. From the angle gathers (Fig. 11) and the initial models (Fig. 12), it can be seen that there is a significant change around 1.8 s.

Fig. 13(a)–(c) display the inverted results of Vp, Vs, and density using SSMI. It can be seen that the resolution is improved compared with the initial model, which can reveal stratigraphic changes. However, the resolution is still very low at the top as well as in the middle, and the layer boundaries are blurred, which does not reflect the details of the subsurface stratigraphy and makes the explanation that follows difficult. Figs. 14 and 15 display the inverted Vp, Vs, and density using MHDS and DHDS, respectively. From the inversion results (Figs. 14 and 15), we can clearly notice that the hybrid-driven strategy can remarkably boost the resolution of the inversion. Compared with the results (Fig. 15) of the DHDS, however, the limitations of MDRI lead

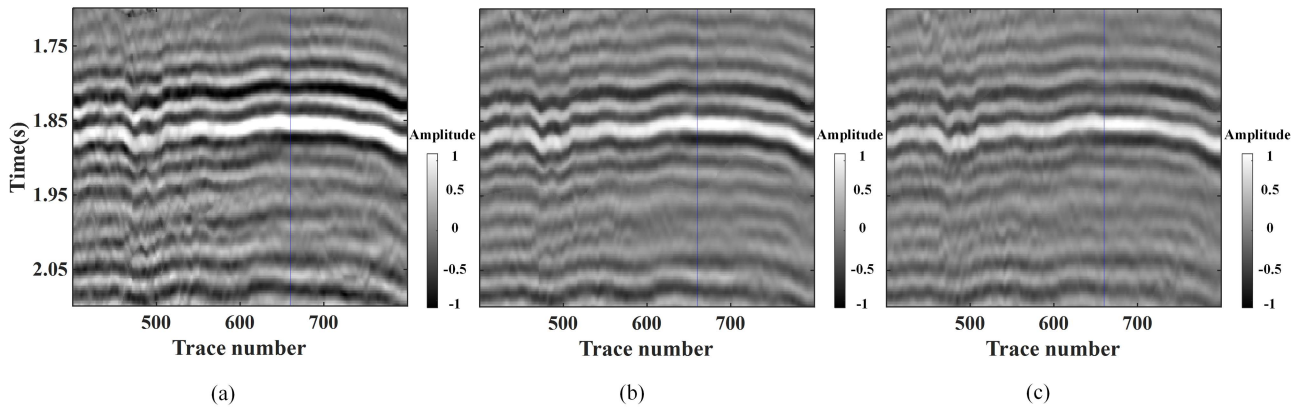

Fig. 11. Real case test (a) small-angle gathers in the range 0°–10°, (b) middle-angle gathers in the range 10°–20°, and (c) large-angle gathers in the range 20°–30°. The blue line marks the position of the well-logs.

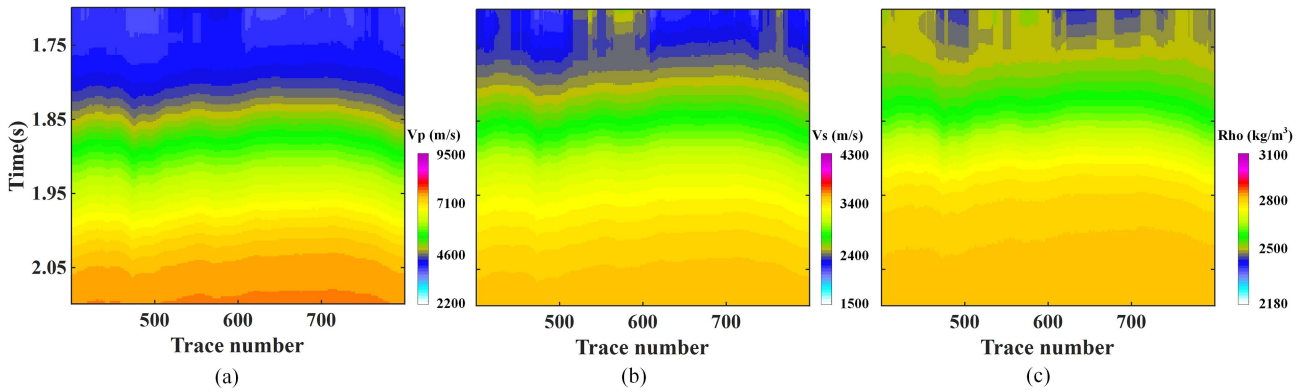

Fig. 12. Initial models of (a) Vp, (b) Vs, and (c) density.

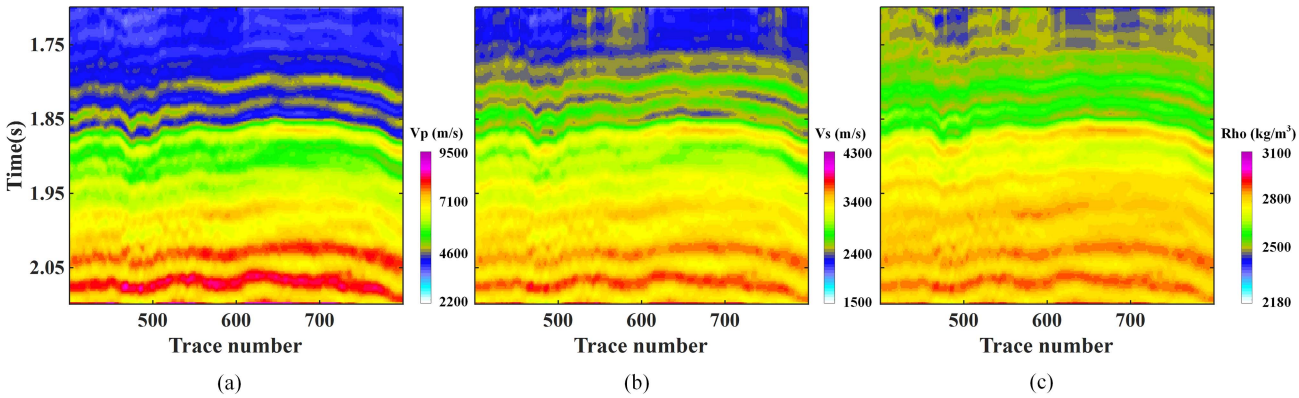

Fig. 13. Inverted results of SSMI (a) Vp, (b) Vs, and (c) density.

to the inverted Vp, Vs, and density of MHDS (Fig. 14) with low resolution and poor stability. This is in accordance with the summary drawn from the synthetic tests. Furthermore, we depict a comparison (Fig. 16) between the well-logs and the inversion results. The red solid lines represent the reference values, the black solid lines with solid dot represent the initial model, the orange dotted lines with solid dot represent the inverted results of SSMI, the blue dashed lines represent the inverted results of MHDS, the green dashed-dotted lines represent the inverted results of DHDS. The inversion results of all three methods can roughly match the well-logs data, but the inversion results of DHDS are the best match to the well-logs data. Table III lists the RMSE between the blind well-logs and the inverted Vp, Vs, and density of SSMI, MHDS, and DHDS. It is clear that the RMSEs between the reference values and the inversion results of DHDS are the smallest. Overall, a sequence of experiments has

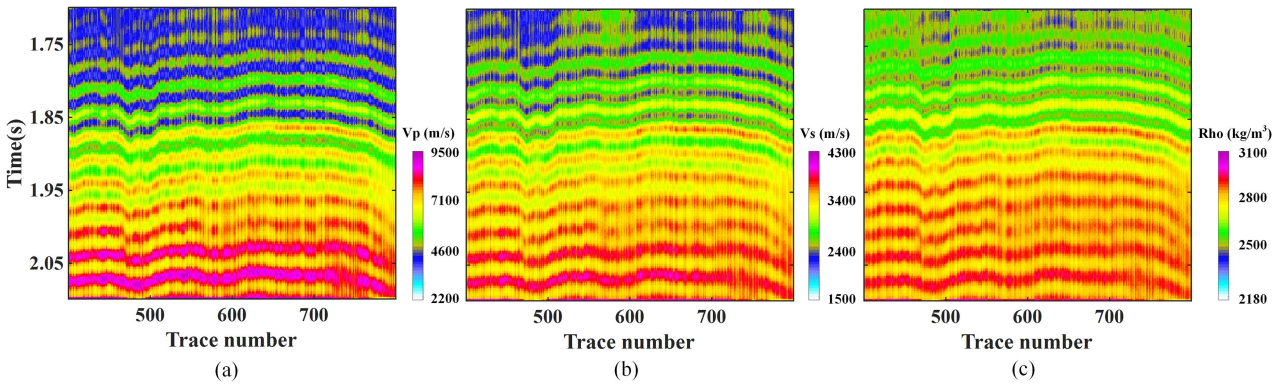

Fig. 14. Inverted results of MHDS (a) Vp, (b) Vs, and (c) density.

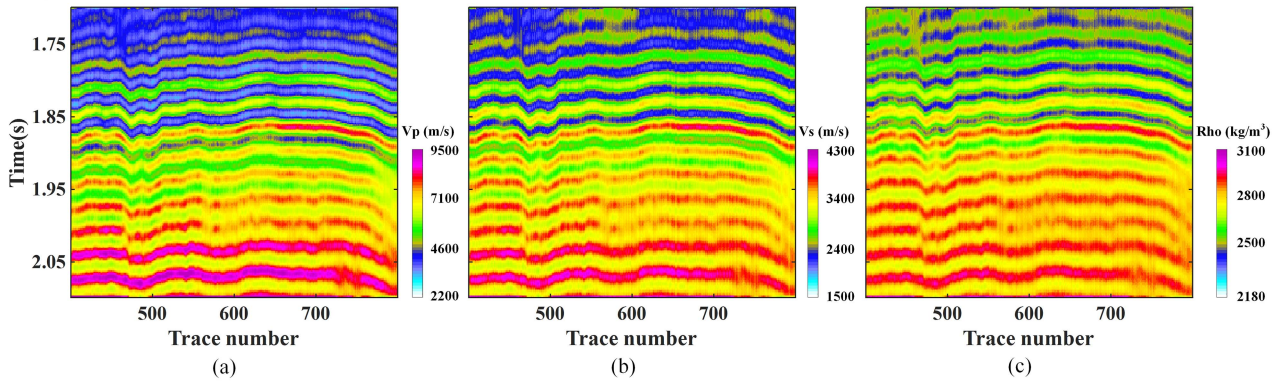

Fig. 15. Inverted results of DHDS (a) Vp, (b) Vs, and (c) density.

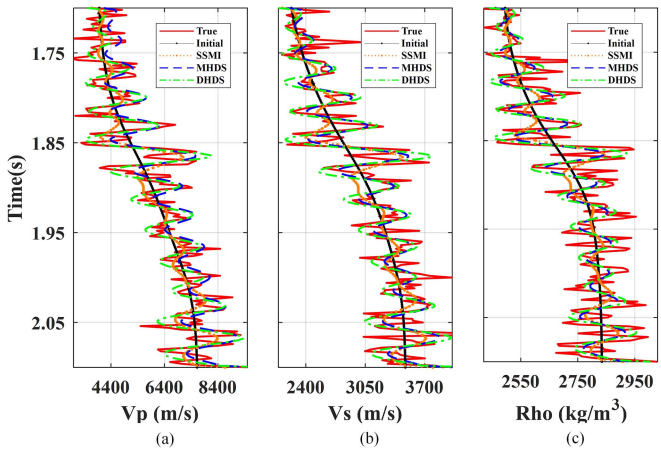

Fig. 16. Comparison of inversion results with true data at the well-site. (a) Inverted Vp using SSMI, MHDS, and DHDS. (b) Inverted Vs using SSMI, MHDS, and DHDS. (c) Inverted density using SSMI, MHDS, and DHDS.

TABLE III
RMSE BETWEEN THE TRUE AND THE INVERTED RESULTS OBTAINED FROM SSMI, MHDS, AND DHDS FOR THE BLIND WELL-LOGS DATA

	Vp	Vs	Rho
SSMI	731.35	234.71	82.95
MHDS	649.72	205.59	72.32
DHDS	582.56	185.43	64.48

qualitatively and quantitatively demonstrated that DHDS has the best performance.

IV. DISCUSSION

Poor robustness of the 2D profiles derived from combining trace-by-trace inversion results in the presence of noise (e.g., noisy or lateral discontinuity), which can prevent many details from being revealed and make interpretation difficult. Transforming the reflectivity to elastic parameters will amplify the lateral discontinuity linked to the different precisions of the reflectivity for different traces. In this article, we perform the inversion trace-by-trace, and the inverted results of HDS depend heavily on the accuracy of the reflectivity. The more accurate the predicted reflectivity, the more stable the predicted Vp, Vs, and density will be. Although DHDS gives more stable results than MHDS, it does not completely solve the problem of lateral discontinuity. Multitrace inversion [37] and edge-preserving smoothing [38] may be good options for further improving the transversal continuity of the inversion while maintaining the resolution of the inversion results.

The stochastic inversion method is another good strategy to enhance the resolution of the inverted results. Figs. 17 and 18 show the inversion results using the stochastic inversion method (i.e., MCMC) and the proposed method, respectively. In the noise-free case, both methods obtain similar results and match

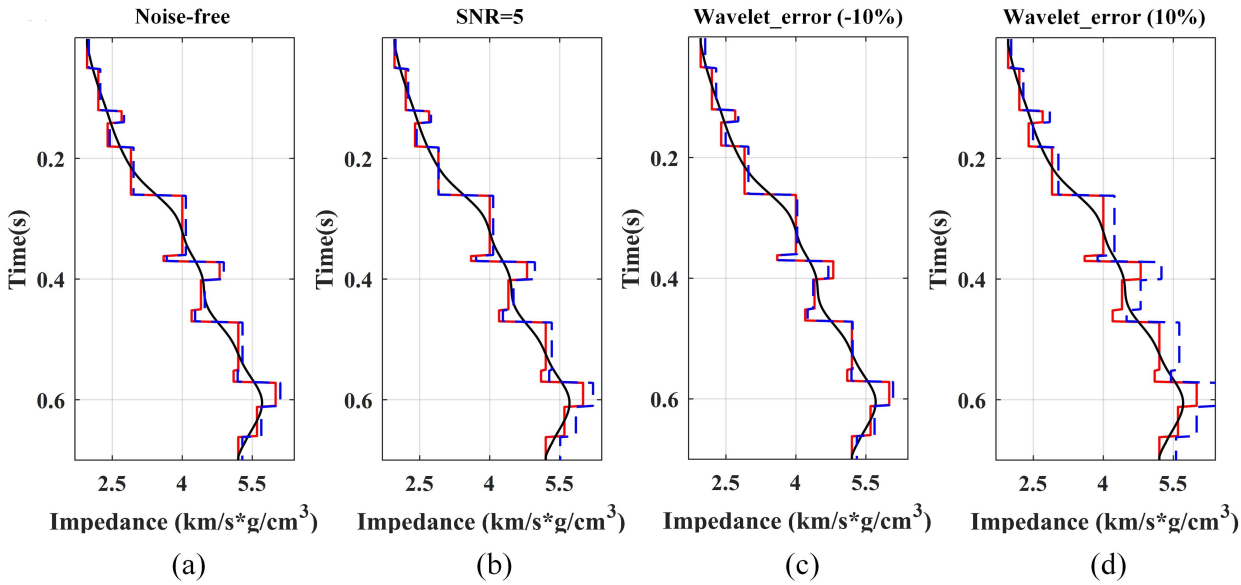

Fig. 17. Inverted results obtained using MCMC.

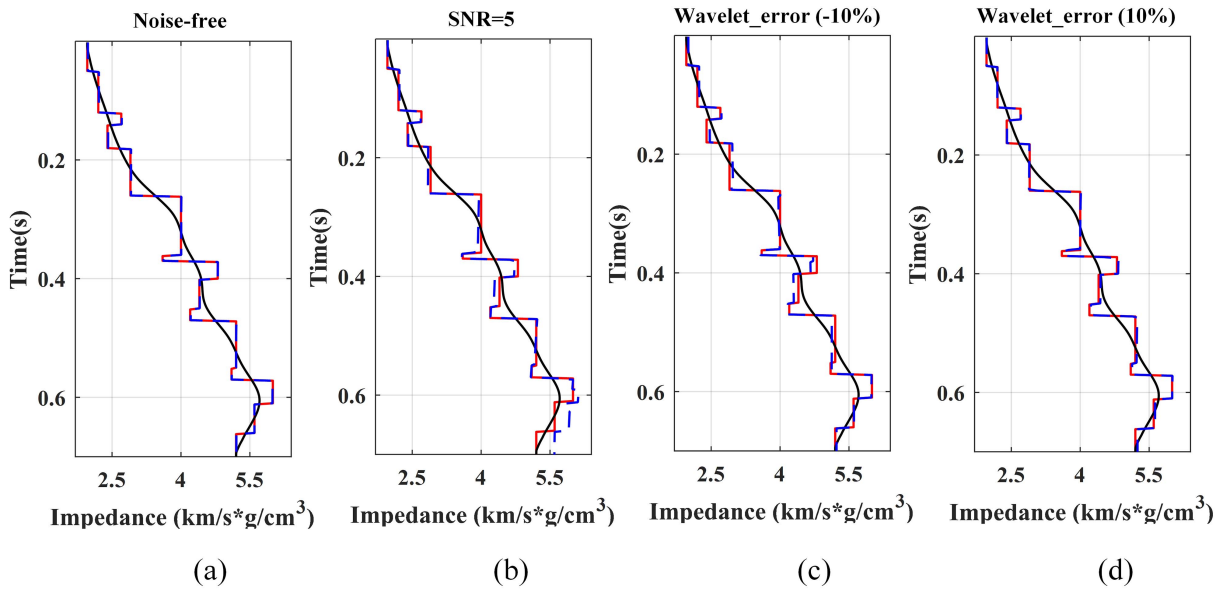

Fig. 18. Inverted results obtained using the proposed method.

well with the true. However, the proposed method is minimally influenced by wavelet compared with the MCMC method. Furthermore, the time cost difference between MCMC (1.5 s) and the proposed (18 ms) is significant. This work provides a good alternative for the prediction of high-resolution elastic parameters.

V. Conclusion

The proposed method combines the advantages of data-driven and model-driven methods to produce high-resolution and stable inversion results of elastic parameters. We demonstrate the proposed methodology on synthetic model and field data. SSMI is adversely affected by wavelet, and the inversion results have low resolution, and the layer boundaries are blurred, which makes subsequent interpretation difficult. The limitations of the MDRI (e.g., strong wavelet dependence) lead to poor stability and low accuracy of the reflectivity, the inverted elastic parameters (i.e., Vp, Vs, and density) of MHDS thus become less accurate and unstable. The DDRI method obtains more reliable reflectivity, allowing the reconstructed elastic parameters of DHDS to match better with the true model. A series of both qualitative and quantitative comparing the inversion results of the SSMI, MHDS, and DHDS show that DHDS outperforms SSMI and MHDS. The inversion results of DHDS provide a more reliable evidence for the subsequent interpretation.

ACKNOWLEDGMENT

The authors would like to thank the Editor Jun Li and three anonymous reviewers for a thorough reading and comments, which significantly improved this article.

REFERENCES

[1] A. Buland and H. Omre, "Bayesian linearized AVO inversion," *Geophysics*, vol. 68, no. 1, pp. 185–198, 2003.
[2] M. Cyz and L. Azevedo, "Direct geostatistical seismic amplitude versus angle inversion for shale rock properties," *IEEE Trans. Geosci. Remote Sens.*, vol. 59, no. 6, pp. 5335–5344, Jun. 2021.
[3] L. Zhou et al., "Robust AVO inversion for the fluid factor and shear modulus," *Geophysics*, vol. 86, no. 4, pp. R471–R483, 2021.
[4] P. Wang et al., "Joint probabilistic fluid discrimination of tight sandstone reservoirs based on Bayes discriminant and deterministic rock physics modeling," *J. Petroleum Sci. Eng.*, vol. 191, 2020, Art. no. 107218.
[5] E. A. Robinson, "Seismic time-invariant convolutional model," *Geophysics*, vol. 50, no. 12, pp. 2742–2751, 1985.
[6] K. Zoeppritz, "On the reflection and propagation of seismic waves," *Gottinger Nachrichten*, vol. 1, no. 5, pp. 66–84, 1919.
[7] D. O. Pérez, D. R. Velis, and M. D. Sacchi, "High-resolution prestack seismic inversion using a hybrid FISTA least-squares strategy," *Geophysics*, vol. 78, no. 5, pp. R185–R195, 2013.
[8] P. G. Richards and K. Aki, *Quantitative Seismology: Theory and Methods*. San Francisco, CA, USA: Freeman, 1980.
[9] R. Shuey, "A simplification of the Zoeppritz equations," *Geophysics*, vol. 50, no. 4, pp. 609–614, 1985.
[10] F. L. Bordignon, L. P. de Figueiredo, L. Azevedo, A. Soares, M. Roisenberg, and G. S. Neto, "Hybrid global stochastic and Bayesian linearized acoustic seismic inversion methodology," *IEEE Trans. Geosci. Remote Sens.*, vol. 55, no. 8, pp. 4457–4464, Aug. 2017.
[11] R. Nunes et al., "Geostatistical seismic inversion with direct sequential simulation and co-simulation with multi-local distribution functions," *Math. Geosci.*, vol. 49, no. 5, pp. 583–601, 2017.
[12] J. Zhang et al., "Geological structure-guided hybrid MCMC and Bayesian linearized inversion methodology," *J. Petroleum Sci. Eng.*, vol. 199, 2021, Art. no. 108296.
[13] W. Alemie and M. D. Sacchi, "High-resolution three-term AVO inversion by means of a Trivariate Cauchy probability distribution," *Geophysics*, vol. 76, no. 3, pp. R43–R55, 2011.
[14] U. Theune, I. Ø. Jensås, and J. Eidsvik, "Analysis of prior models for a blocky inversion of seismic AVA data," *Geophysics*, vol. 75, no. 3, pp. C25–C35, 2010.
[15] K. Gao and L. Huang, "Acoustic-and elastic-waveform inversion with total generalized p-variation regularization," *Geophysical J. Int.*, vol. 218, no. 2, pp. 933–957, 2019.
[16] G. Huang, X. Chen, and Y. Chen, "P-P and dynamic time warped P-SV wave AVA joint-inversion with $\ell_{1\text{-}2}$ regularization," *IEEE Trans. Geosci. Remote Sens.*, vol. 59, no. 7, pp. 5535–5548, Jul. 2021.
[17] D. A. Cooke and W. A. Schneider, "Generalized linear inversion of reflection seismic data," *Geophysics*, vol. 48, no. 6, pp. 665–676, 1983.
[18] A. Walden and J. Hosken, "The nature of the non-Gaussianity of primary reflection coefficients and its significance for deconvolution," *Geophysical Prospecting*, vol. 34, no. 7, pp. 1038–1066, 1986.
[19] S. Yuan and S. Wang, "Spectral sparse Bayesian learning reflectivity inversion," *Geophysical Prospecting*, vol. 61, no. 4, pp. 735–746, 2013.
[20] F. Li, R. Xie, W.-Z. Song, and H. Chen, "Optimal seismic reflectivity inversion: Data-driven ℓ_p-loss-ℓ_q-regularization sparse regression," *IEEE Geosci. Remote Sens. Lett.*, vol. 16, no. 5, pp. 806–810, May 2019.
[21] X. Xu, J. Gao, B. Zhang, H. Chen, and Y. Yang, "Multichannel reflectivity inversion with sparse group regularization based on HPPSG algorithm," *IEEE Geosci. Remote Sens. Lett.*, vol. 17, no. 5, pp. 784–788, May 2020.
[22] S. S. Chen, D. L. Donoho, and M. A. Saunders, "Atomic decomposition by basis pursuit," *SIAM Rev.*, vol. 43, no. 1, pp. 129–159, 2001.
[23] D. P. Wipf and B. D. Rao, "Sparse Bayesian learning for basis selection," *IEEE Trans. Signal Process.*, vol. 52, no. 8, pp. 2153–2164, Aug. 2004.
[24] Y. LeCun, Y. Bengio, and G. Hinton, "Deep learning," *Nature*, vol. 521, no. 7553, pp. 436–444, 2015.
[25] O. M. Saad and Y. Chen, "Deep denoising autoencoder for seismic random noise attenuation," *Geophysics*, vol. 85, no. 4, pp. V367–V376, 2020.
[26] D. Liu et al., "Accelerating seismic scattered noise attenuation in offset-vector tile domain: Application of deep learning," *Geophysics*, vol. 87, no. 5, pp. V505–V519, 2022.
[27] D. Liu, Z. Deng, C. Wang, X. Wang, and W. Chen, "An unsupervised deep learning method for denoising prestack random noise," *IEEE Geosci. Remote Sens. Lett.*, vol. 19, 2022, Art. no. 7500205.
[28] J. Zhang et al., "Robust deep learning seismic inversion with a priori initial model constraint," *Geophysical J. Int.*, vol. 225, no. 3, pp. 2001–2019, 2021.
[29] X. Liu et al., "Quantitative characterization of shale gas reservoir properties based on BiLSTM with attention mechanism," *Geosci. Front.*, vol. 14, no. 4, 2023, Art. no. 101567.
[30] X. Liu et al., "Simulation of complex geological architectures based on multi-stage generative adversarial networks integrating with attention mechanism and spectral normalization," *IEEE Trans. Geosci. Remote Sens.*, vol. 61, 2023, Art. no. 5913215.
[31] D. Liu et al., "Improving vertical resolution of vintage seismic data by a weakly supervised method based on Cycle GAN," *Geophysics*, vol. 88, no. 6, pp. 1–103, 2023.
[32] A. Pochet, P. H. B. Diniz, H. Lopes, and M. Gattass, "Seismic fault detection using convolutional neural networks trained on synthetic post-stacked amplitude maps," *IEEE Geosci. Remote Sens. Lett.*, vol. 16, no. 3, pp. 352–356, Mar. 2019.
[33] J. Zhang, J. Li, X. Chen, Y. Li, and W. Tang, "A spatially coupled data-driven approach for lithology/fluid prediction," *IEEE Trans. Geosci. Remote Sens.*, vol. 59, no. 7, pp. 5526–5534, Jul. 2021.
[34] X. Liu et al., "Deep classified autoencoder for lithofacies identification," *IEEE Trans. Geosci. Remote Sens.*, vol. 60, 2022, Art. no. 5909914.
[35] X. Liu et al., "Stochastic simulation of facies using deep convolutional generative adversarial network and image quilting," *Mar. Petroleum Geol.*, vol. 146, 2022, Art. no. 105932.
[36] Y. Shi, X. Wu, and S. Fomel, "Waveform embedding: Automatic horizon picking with unsupervised deep learning," *Geophysics*, vol. 85, no. 4, pp. WA67–WA76, 2020.
[37] J. Zhang et al., "Structure-oriented pre-stack waveform inversion," *Geophysics*, vol. 87, no. 3, pp. M73–M85, 2022.
[38] R. Dai et al., "Seismic inversion with adaptive edge-preserving smoothing preconditioning on impedance model," *Geophysics*, vol. 84, no. 1, pp. R11–R19, 2019.

Jian Zhang received the B.Sc. degree in geophysics from Northeast Petroleum University, Daqing, China, in 2016, and the Ph.D. degree in geophysics from the China University of Petroleum-Beijing, Beijing, China, in 2021.

He is currently an Associate Professor with the Faculty of Geosciences and Environmental Engineering, Southwest Jiaotong University, Chengdu, China. His research interests include seismic data inversion, deep learning, reservoir characterization and evaluation, and nonlinear parameter estimation.

Xiaoyan Zhao received the B.Sc. degree in geological engineering and the Ph.D. degree in geotechnical engineering from Southwest Jiaotong University, Chengdu, China, in 2000 and 2005, respectively.

He is currently a Professor with the Faculty of Geosciences and Environmental Engineering, Southwest Jiaotong University. His research interests include signal processing, slope instability mechanism, reinforcement, and geologic characterization.

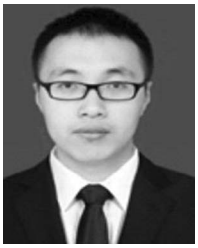

Hui Sun received the B.S. and Ph.D. degrees in geophysics from Jilin University, China, in 2011 and 2017, respectively.

From 2018 to 2019, he was engaged in Postdoctoral Research with the University of California, Santa Cruz (UCSC). He is currently an Associate Professor with the Faculty of Geosciences and Environmental Engineering, Southwest Jiaotong University, Chengdu, China. His research interests include seismic signal processing, seismic imaging methods, and forward modeling.

Jingye Li received the B.Sc. degree in geological engineering and the Ph.D. degree in geophysics from the China University of Petroleum-Beijing, Beijing, China, in 2001 and 2005, respectively.

He is currently a Professor with Geophysical Exploration Department, China University of Petroleum-Beijing. His research interests include seismic data processing and reservoir geophysics.

Dr. Li was the recipient of the Sun Yueqi Young Scientist Award and the Liu Guangding Young Geophysicist Award.

Xiaohong Chen received the B.S. degree in mathematics from Nanjing University, Nanjing, China, in 1982, the M.S. degree in applied mathematics from Harbin Institute of Technology, Harbin, China, in 1988, and the Ph.D. degree in applied geophysics from the China University of Petroleum, Beijing, China, in 1993.

In 1997, he was a Visiting Scholar with Columbia University and is currently a Professor in applied geophysics with the China University of Petroleum, Beijing, China. His research interests include signal processing, seismic inversion, and time-lapse seismic reservoir monitoring.